  DOI 10.1515/htmp-2012-0057

Effective Temperature of High Pressure Torsion in Zr-Nb Alloys

Boris B. Straumal,[1,2,*] **Alena S. Gornakova,**[1] **Olga B. Fabrichnaya,**[3] **Mario J. Kriegel,**[3] **Andrey A. Mazilkin,**[1,2] **B. Baretzky,**[2] **A. M. Gusak**[4] **and S. V. Dobatkin**[5]

[1] Institute of Solid State Physics, Russian Academy of Sciences, Chernogolovka

[2] Karlsruher Institut für Technologie, Institut für Nanotechnologie, Eggenstein-Leopoldshafen

[3] TU Bergakademie Freiberg, Institut für Werkstoffwissenschaft, Freiberg

[4] Cherkasy National University, Cherkasy

[5] A. A. Baikov Institute of Metallurgy and Materials Science, Russian Academy of Sciences, Moscow

Abstract. Severe plastic deformation by the high pressure torsion (HPT) leads to the phase transitions and strong grain refinement. The starting α Zr-phase in Zr alloyed by 2.5 and 8 mass% Nb transforms into $\beta + \omega$ mixture. This $\beta + \omega$ phase mixture can be found in the equilibrium phase diagram at higher (effective) temperature ($T_{\text{eff}} = 620$°C for Zr-2.5 mass% Nb and $T_{\text{eff}} = 550$°C for Zr-8 mass% Nb). The published papers on phase transitions during HPT are analysed and the values of effective temperature are estimated. Contrary to the increasing temperature, the increasing pressure slows down the diffusion and grain boundary migration. Therefore, the forced atomic movement during HPT produces the states equivalent to higher temperature, but not to the higher pressure.

Keywords. Nanocrystalline materials, high pressure torsion, phase transitions, Zr-Nb alloys.

PACS®(2010). 64.70.Kb.

1 Introduction

It has been demonstrated recently that concept of effective temperature originally proposed for the materials under severe irradiation [1] is applicable also for severe plastic deformation (SPD) [2]. If the atomic movements driven by an external action (deformation or irradiation) are higher in comparison with the conventional thermal diffusion, the material is forced to undergo into the state which is equivalent to the state at a certain increased (effective) temperature T_{eff}. One can estimate T_{eff} if the phases in a material after SPD treatment differ from those before SPD [2]. This method is quite productive since SPD frequently leads to the phase transformations [3] e.g. the formation [4–12] or decomposition [13–15] of a supersaturated solid solution, dissolution of phases [16–28], disordering of ordered phases [19–31], amorphyzation of crystalline phases [32–40], synthesis of the low-temperature [21, 28], high-temperature [41–43] or high-pressure [44–52] allotropic modifications, and nanocrystallization in the amorphous matrix [53–61]. Some of these phase transformation need only a small shift of atoms, for other ones the long-range mass transfer is needed. The results of such SPD-driven transitions cannot be explained by the bulk or even grain boundary diffusion at the SPD temperature (which usually remains slightly above ambient one).

It is rather easy to estimate the T_{eff} if one can find the phases existing in a material before and after SPD in an equilibrium "temperature-composition" phase diagram. But it becomes a real challenge if the high-pressure phases appear during SPD. The good object for such experiments is the titanium group of elements (Ti, Zr, and Hf). Ti, Zr, and Hf all have the hcp crystal structure (α-phase) at room temperature and zero pressure. At high temperature and zero pressure they transform to the bcc structure (β-phase) before reaching the melting temperature [62]. At room temperature and under pressure they undergo a crystallographic phase change into the so-called ω-structure [63–77]. At even higher pressures both Zr and Hf have been observed to transform to the bcc structure (β-phase) [67, 68, 75, 76].

Zr-Nb alloys play an important role in the energy production being the main material for the cladding of nuclear fuel in the nuclear power plants [78, 79]. Most common are the Zr-2.5 mass% Nb alloys. Zr-Nb alloys are also useful for medical applications [80]. SPD by high-pressure torsion (HPT) permits to obtain the extremely fine-grained structure in Zr and Zr alloys [46–50, 77]. They contain also the high pressure ω-phase which remains quenched after release of high pressure. The ω-phase appears after SPD also in Ti but not in Hf [49, 52, 81]. If one compares the phases in Zr, Ti and Hf alloys before and after SPD with the equilibrium high-pressure phase diagrams, one can estimate the effective temperature during SPD treatment [2]. The investigation of phase transformations in the HPT-treated Zr-Nb

* **Corresponding author:** Boris B. Straumal, Institute of Solid State Physics, Russian Academy of Sciences, Ac. Ossipyan str. 2, Chernogolovka, 142432, Russia; Karlsruher Institut für Technologie, Institut für Nanotechnologie, Hermann-von-Helmholtz-Platz 1, 76344 Eggenstein-Leopoldshafen, Germany;
E-mail: straumal@mf.mpg.de.

Received: June 03, 2012. Accepted: June 16, 2012.

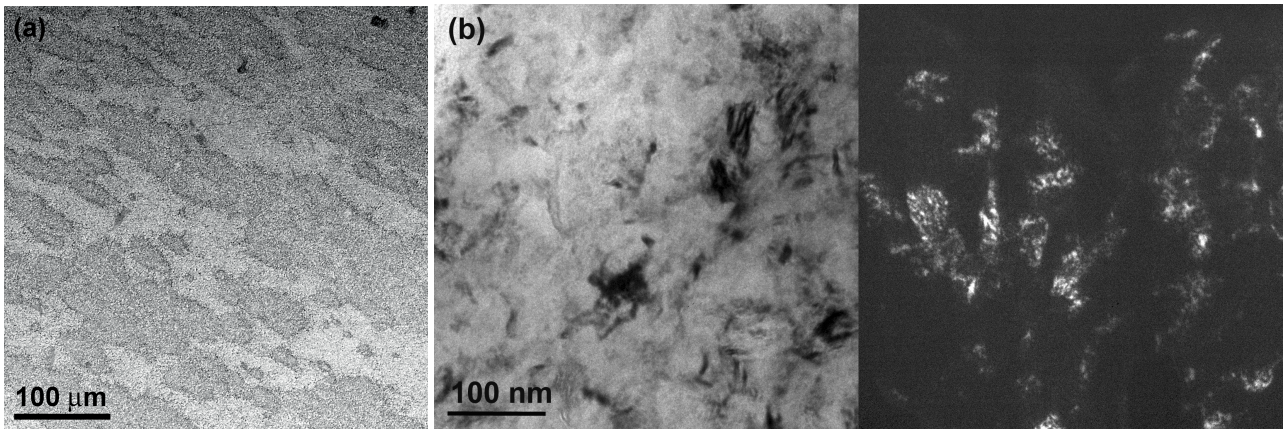

Figure 1. (a) SEM micrograph of the as-cast Zr-2.5 mass% Nb alloy. (b) bright field (left) and dark field (right) TEM micrographs of the HPT-treated Zr-8 mass% Nb alloy.

alloys and the comparison with Ti and Hf alloys was the goal of this work.

2 Experimental

The Zr-Nb alloys with 2.5 and 8 mass% Nb were investigated. The alloys were prepared of high purity components (4N Zr and 4N Nb) by the vacuum induction melting. The melt was poured in the vacuum into the water-cooled cylindrical copper crucible of 10 mm diameter. After sawing, grinding, and chemical etching, the 0.7 mm thick disks cut from the as cast cylinders were subjected to HPT in a Bridgman anvil type unit (room temperature, pressure 5 GPa, 5 torsions, 1 rotation-per-minute). After HPT, the central (low-deformed) part of each disk (about 3 mm in diameter) was excluded from further investigations. The samples for structural investigations and calorimetry were cut from the deformed disks at a distance of 4–5 mm from the sample center. For this distance the shear strain is ~ 6. The 2 mm thick slices were also cut from the cylindrical ingots, then divided into four parts. After quenching, samples were embedded in resin and then mechanically ground and polished, using 1 μm diamond paste in the last polishing step, for the metallographic study. After etching, samples were investigated by means of the light microscopy (LM) and by scanning electron microscopy (SEM). SEM investigations have been carried out in a Tescan Vega TS5130 MM microscope equipped with the LINK energy-dispersive spectrometer produced by Oxford Instruments. LM has been performed using a Neophot-32 light microscope equipped with a 10 Mpix Canon Digital Rebel XT camera. The samples for TEM investigations were prepared by ion milling on the PIPS machine. TEM investigations were carried out on a TECNAI F2 electron microscope with acceleration voltage of 200 kV. The dark field image was taken in the most bright reflection to which contribute both α and ω phases. X-ray diffraction (XRD) data were obtained on a Siemens diffractometer (Co K_{ff} radiation). Grain size was estimated by the XRD line broadening and using the Scherer formula [82]. Both the as-cast coarse-grained CG and fine-grained HPT-samples were studied with the aid of differential scanning calorimetry (DSC) using the NETZSCH Pegasus 404C calorimeter in the dry argon atmosphere, Al_2O_3 crucibles and at the cooling and heating rates of 20 K/min. In order to record the DSC curves, the samples were heated from 100 to 900°C. Thermodynamic calculations were performed using thermodynamic data of Guillermet [83] where solid solutions bcc and hcp as well as liquid solution were described by substitutional model. The bcc phase was described as single phase which forms miscibility gap in the composition range from 8 to 81 mass% Zr and temperatures from 620 up to 976°C. Thermo-calc software [84] was used to calculated equilibrium phase diagrams and diffusionless transformation hcp↔bcc.

3 Results

Figure 1a shows the SEM micrograph of the as-cast Zr-2.5 mass% Nb alloy. The grain size in both CG as-cast alloys determined with the aid of SEM and LM was about 100–300 μm. Figure 1b shows the bright field and dark field TEM micrograph of the HPT-treated Zr-8 mass% Nb alloy. HPT drastically refined the grains. Both Zr-Nb alloys became ultra-fine grained (UFG). Grain size of the ωZr after HPT estimated for (111) reflection in XRD was about 14 nm and 7 nm for the alloys with 2.5 mass% and 8 mass% Nb, respectively (Figure 2). As to the βZr, its grain size was estimated after the deconvolution of the corresponding peaks, as they are overlapped with those from α and ω phases. Calculations gave the values of 24 nm and 11 nm for the alloys with 2.5 mass% and 8 mass% Nb, respectively.

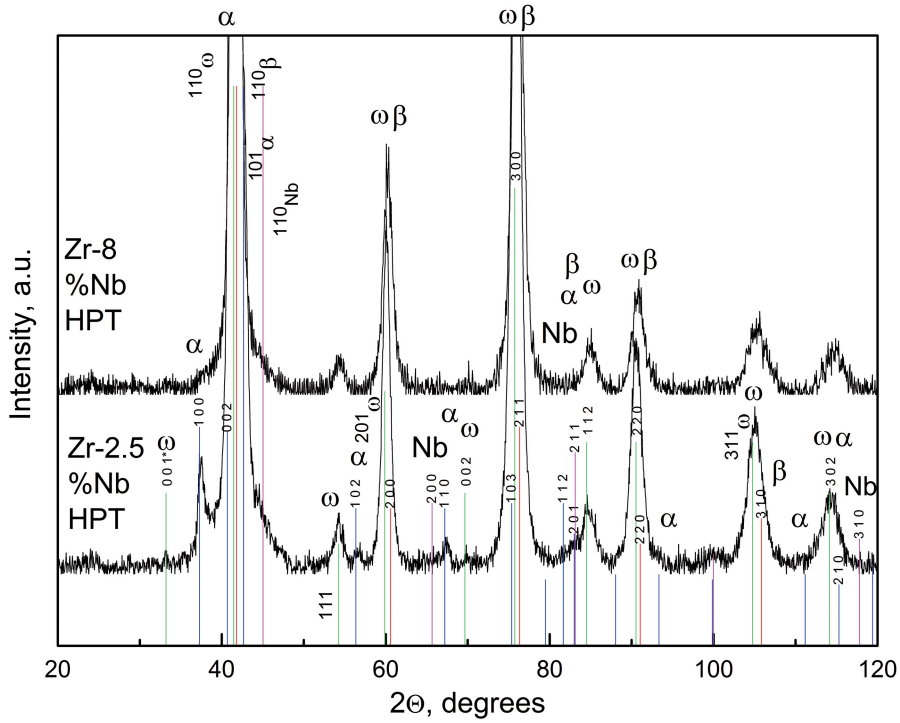

Figure 2. XRD curves for the UFG Zr-2.5 mass% Nb and UFG Zr-8 mass% Nb allos after HPT.

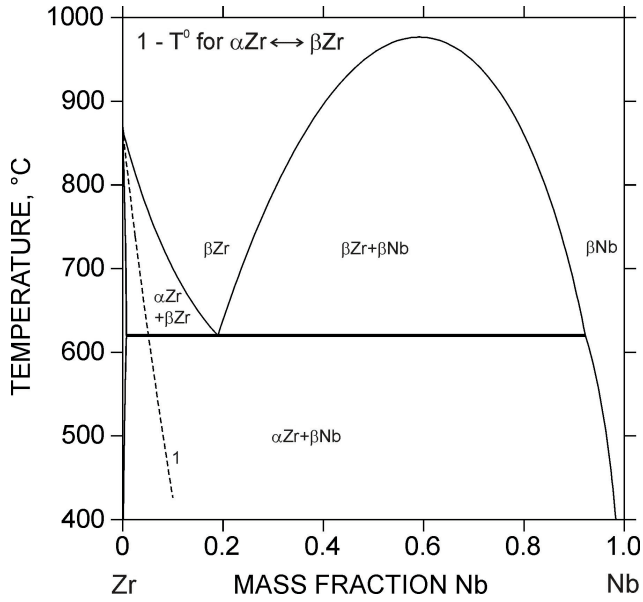

Figure 3. The part of the Zr-Nb equilibrium phase diagram. Dashed line shows the martensitic martensitic αZr$\leftrightarrow$ βZr transformation.

XRD-spectra of CG as-cast alloys demonstrate that they contain mainly αZr with hexagonal closely-packed lattice. The Nb-rich body-centered cubic phase is absent. Small amount of βZr is present in the CG as-cast alloys. Nb-poor βZr has a body-centered cubic lattice and is isomorhous to the Nb-rich bcc-phase. The calculated phase diagram (Figure 3) reproduces experimental data [62] very well. Below the temperature of a monotectoid transformation $T_{\text{mon}} = 620$°C the stable assemblage is βNb + αZr according to the Zr-Nb phase diagram (Figure 3). Above monotectoid reaction and composition Nb <19 mass%, βZr is in equilibrium with αZr phase which transforms to βZr single phase with temperature increase. For compositions with Nb > 19 mass% and temperatures between monotectoid reaction and critical point $T_{\text{c}} = 976$°C a two-phase area βZr + βNb (Figure 3) exists. After HPT both fine-grained Zr-Nb alloys contain mainly the ωZr phase (Figure 2). The ωZr phase possesses the hexagonal C32 structure [86]. At the diffraction angle $2\Theta = 54°$ the peak of a ωZr (C32) phase is clearly visible without overlapping with peaks of other phases. αZr (hcp-phase) almost disappeared after HPT. The Nb-rich (βNb -phase) is absent both after and before HPT. All diffraction peaks of the βZr phase are very close to the peaks of ωZr (C32) phase (Figure 2). Nevertheless, the positions of the diffraction peaks at $2\Theta = 60°$, 76°, 91° and 105° for the Zr-2.5 mass% Nb alloy after HPT almost perfect coincide with tabulated values for the 201, 300, 220-and 311 peaks for the ωZr (C32) phase. In the Zr-2.5 mass% Nb alloy the same diffraction peaks are shifted to the right and are positioned between the respective tabulated values for the ωZr (C32) and βZr phases. In other words, the amount of βZr phase after HPT is much higher in the Zr-2.5 mass% Nb alloy than in the Zr-8 mass% Nb one.

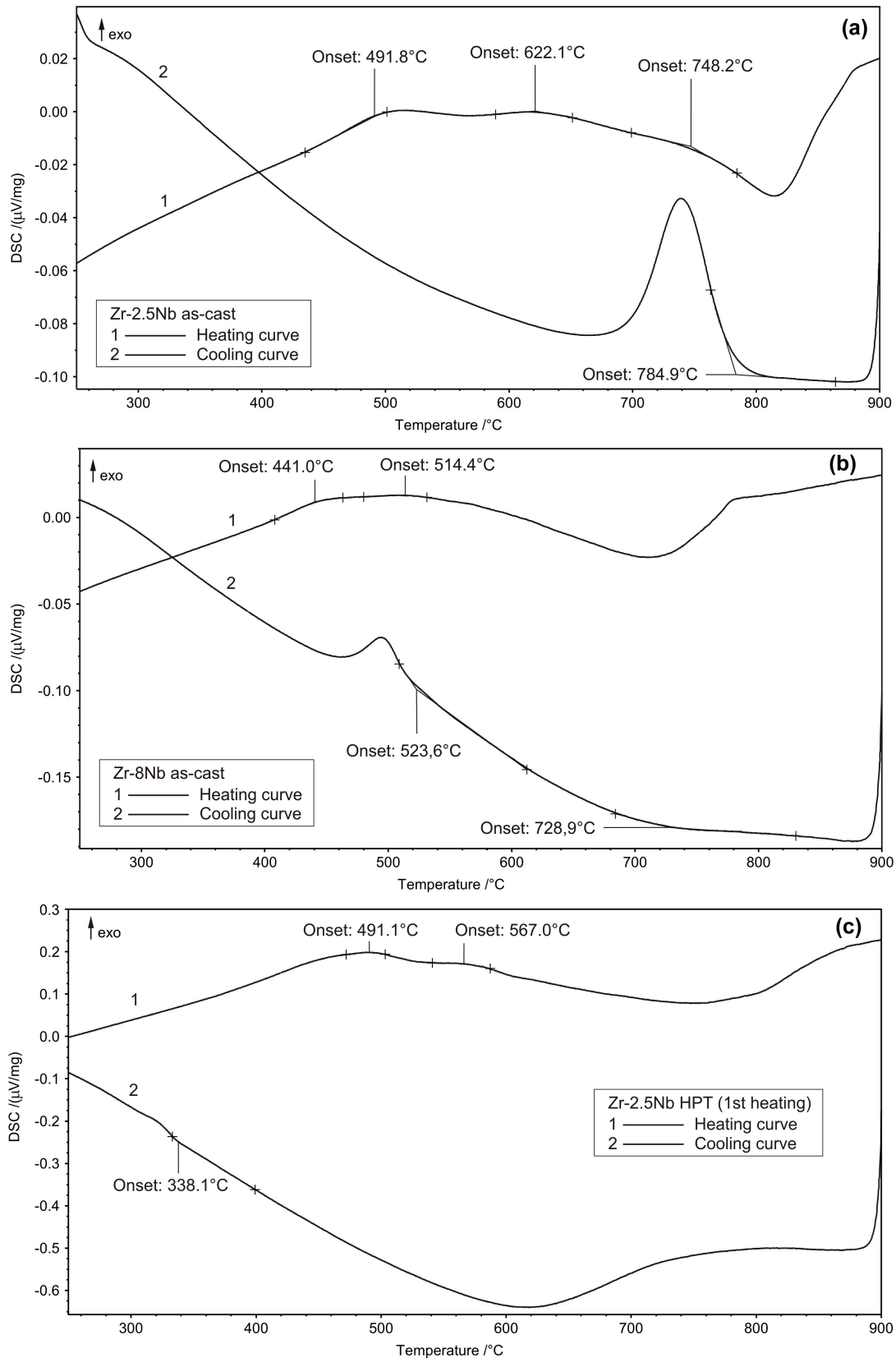

Figure 4. The temperature dependences of heat flow DSC by heating (upper curves) and by cooling (lower curves) for (a) as-cast CG Zr-2.5 mass% Nb alloy, (b) as-cast CG Zr-8 mass% Nb alloy and (c) UFG Zr-2.5 mass % Nb alloy after HPT (first heating).

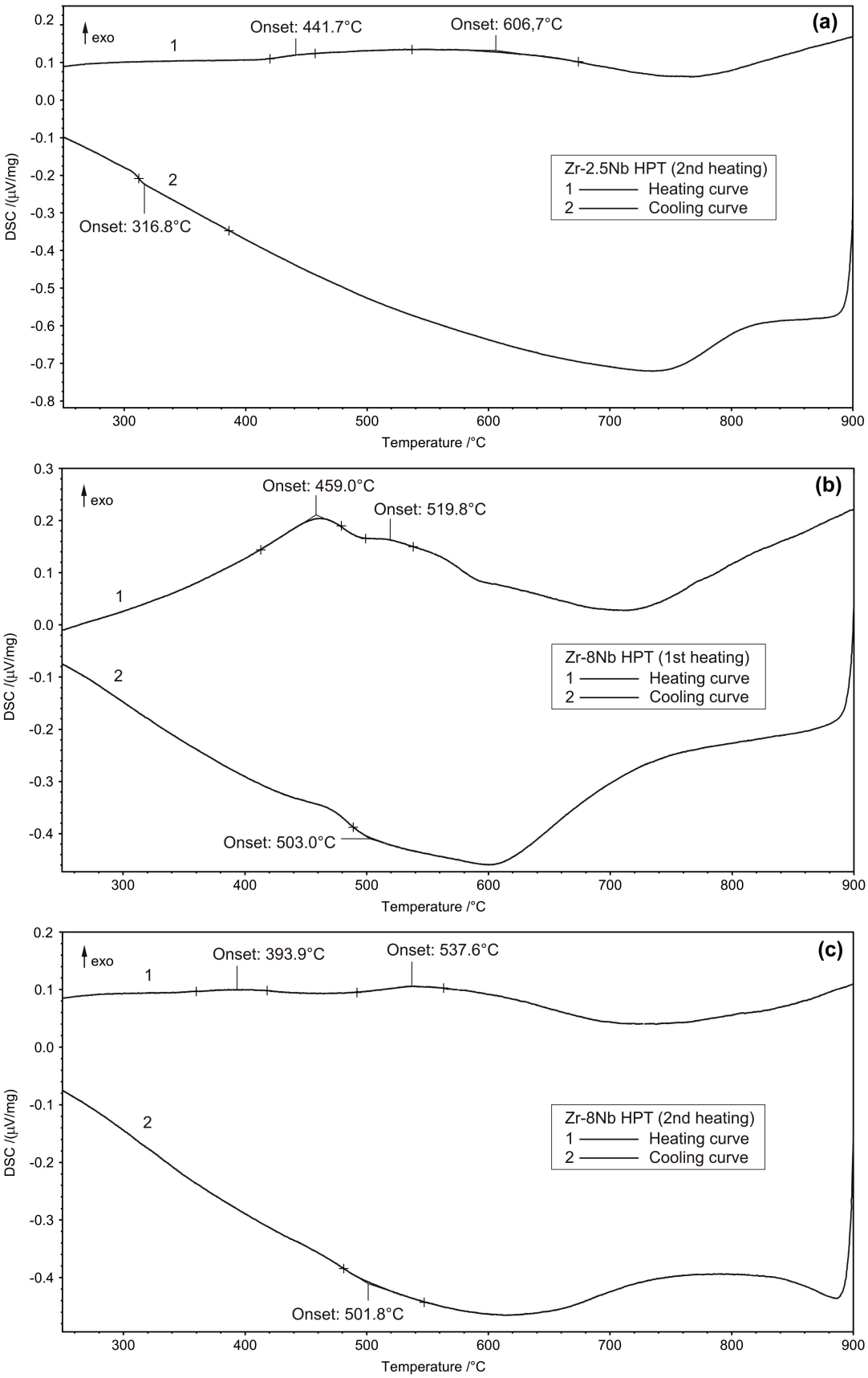

Figure 5. The temperature dependences of heat flow DSC by heating (upper curves) and by cooling (lower curves) for (a) UFG Zr-2.5 mass% Nb alloy after HPT (second heating), (b) UFG Zr-8 mass% Nb alloy after HPT (first heating), (c) UFG Zr-8 mass% Nb alloy after HPT (second heating).

In Figure 4 and Figure 5 the temperature dependences of heat flow (DSC curves) are shown for the as-cast and HPT-treated Zr-Nb alloys. In the as-cast CG Zr-2.5 mass% Nb alloy (Figure 4a) two heat effects are clearly visible. The first one is due to monotectic reaction $\alpha\mathrm{Zr} + \beta\mathrm{Nb} \leftrightarrow \beta\mathrm{Zr}$ (onset at 623.1°C) and the second one is due to change of the $\alpha\mathrm{Zr} + \beta\mathrm{Zr}$ two phase area into single βZr phase field (e.g. Figure 3) around 820°C. These temperatures are very close to the respective ones in the equilibrium Zr-Nb phase diagram (Figure 3). The onset at 491.8°C can be explained by the transformation of retained βZr which is visible in the XRD-spectrum of as-cast CG alloys [87] into equilibrium assemblage $\beta\mathrm{Nb} + \alpha\mathrm{Zr}$, which further transforms to $\beta\mathrm{Zr} + \alpha\mathrm{Zr}$ (622.1°C) up to complete transformation to βZr starting at 748.2°C and showing deep minimum at 820°C. The transformation of βZr to $\alpha\mathrm{Zr} + \beta\mathrm{Zr}$ is indicated on cooling curve (on-set 784.9°C). The temperature of transformation on heating is close to temperature of reverse transformation on cooling. This confirms that both transformations are diffusion controlled. The DSC curve for the as cast Zr-8 mass% Nb alloy looks different (Figure 4b).The non-equilibrium phase βZr found in as-cast Zr-8 mass% Nb alloy transforms into αZr phase at 441.0°C, the following transformation of αZr into βZr occurs as martensitic at 514.4°C. This is in agreement with calculated martensitic transformation shown by dashed line at Figure 3. At further heating martensite βZr continuously transforms into equilibrium assemblage $\alpha\mathrm{Zr} + \beta\mathrm{Zr}$ which finally transforms into stable βZr at 728.9°C corresponding to deep minimum at DSC curve. Only one exothermic effect was observed on cooling at temperature (onset 523.6°C) which is much lower than minimum on heating. This exothermic effect can be attributed to diffusionless transformation of βZr to αZr. The temperature of this effect is in a good agreement with calculated temperature of diffusionless transformation. It should be mentioned that both as-cast samples Zr-2.5 mass% Nb and Zr-8 mass% Nb reproduce their behavior during second heating and cooling.

The curves for the HPT-treated samples are quite different. First, the reaction with a very pronounced heat effect starts at 491.1°C in the Zr-2.5 mass% Nb alloy (Figure 4c) and at 441.7°C in the Zr-8 mass% Nb alloy (Figure 5b). This reaction does not proceed in the repeated DSC-run (Figures 6a and 5c), if the HPT-treated samples are cooled down after first DSC-run and heated again. Therefore, these onset can be attributed with transformation of metastable ωZr into αZr one. It has to be underlined that not only the amount of ωZr is lower in the Zr-8 mass% Nb alloy (compare spectra in Figure 2), but also it transforms to αZr phase at lower temperature. The second feature in alloy Zr-2.5 mass% Nb at 567.0°C can be explained by the transformation of metastable βZr found in HPT treated alloy into αZr phase. The second heat effect for Zr-8 mass% Nb alloy can be explained by diffusionless transformation of αZr to βZr. The calculated dashed line in Figure 3 is for the the martensitic $\alpha \leftrightarrow \beta$ transformation can be used to interpret the DSC curves of HPT-treated alloys. It should be mentioned that all transformations at temperatures below 620°C occur by diffusionless mechanism. The diffusion-controlled transformation from αZr into βZr through the two-phase $\alpha + \beta$ region (e.g. Figure 3) is not visible in the DSC curves for both HPT-treated alloys. Probably equilibrium assemblage $\alpha + \beta$ are continuously forming during heating of martensite αZr or βZr which further transforms to stable single phase βZr. It should be mentioned, it is known the $\alpha \leftrightarrow \beta$ transition in Zr and Ti alloys can proceed as diffusionless martensitic one [88, 89]. The martensite αZr in Zr-2.5 mass% Nb alloy continuously transforms to equilibrium $\alpha\mathrm{Zr} + \beta\mathrm{Zr}$ assemblage which finally transforms to stable single βZr phase showing the deep minima in DSC curves at 750°C in the Zr-2.5 mass% Nb alloy. Martensite βZr in the Zr-8 mass% Nb alloy continuously transforms to equilibrium $\alpha\mathrm{Zr} + \beta\mathrm{Zr}$ assemblage which finally transforms into stable βZr at 710°C. The grain size effect on presence or absence of martensitic transformation has been observed in precipitates in Zr-1 mass% Nb alloy [89]. Therefore, we can suppose that the clear change from diffusional to martensitic transformations in the HPT-treated Zr-Nb alloys in comparison with as-cast alloys could be due to the SPD-driven grain refinement.

4 Discussion

Usually, the high applied pressure decreases the diffusivity and grain boundary mobility [90, 91]. However, the atom movements caused by strong external forces can drive both accelerated diffusion and phase transformations in the material [85]. Historically, such unusual behavior was first observed in the materials under severe irradiation [1]. G. Martin proposed the simplified mean-field description of solid solutions subjected to irradiation-induced atomic mixing [1]. His main idea was that the forced mixing induced by irradiation emulates the increase of entropy and changes the thermodynamic potentials in the alloy. In a simple case of regular solution in the Bragg–Williams approximation a law of corresponding states was formulated: The equilibrium configuration of the solid under irradiation flux φ at temperature T is identical to the configuration at $\varphi = 0$ and a certain effective temperature

$$T_{\mathrm{eff}} = T(1 + \Delta). \tag{1}$$

If the irradiation-driven movements of atoms are similar in amplitude to conventional diffusion jumps, they can be described by the "ballistic" diffusion coefficient D_{ball} and $\Delta = D_{\mathrm{ball}}/D_{\mathrm{b}}$, where D_{b} is conventional bulk diffusion coefficient, possibly increased due to the non-equilibrium defect concentration [1]. It means that one can use the equilibrium phase diagram for the description of the system un-

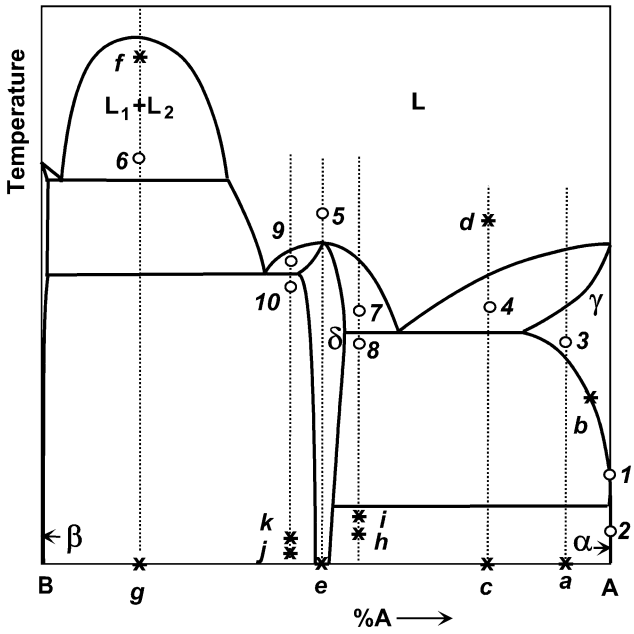

Figure 6. The schematic binary phase diagram showing the points of HPT deformation or other thermal treatments (stars) and respective configuration points at the (increased) effective temperatures. Other explanations are in the text.

der irradiation, but at T_{eff} instead of the actual temperature T. For example, if the liquid phase is present in the phase diagram at T_{eff}, the amorphous phase would appear under irradiation [1, 92].

For checking of the applicability of the Martin's law (1) to the forced diffusion driven by pure shear deformation (D_{HPT}) instead of irradiation (D_{ball}) the experiments where HPT led to the phase transformations have to be analyzed. We chosen for the comparison the data where (i) the HPT-driven atomic movements are comparable with each other, i.e. HPT was performed at 4–6 GPa with 4–6 torsions and (ii) the phases appeared after HPT can be easily localized in the phase diagrams and are different from those present in the samples before HPT.

The composition of the phases after SPD allows to localize those phases in the respective equilibrium phase diagram and to estimate the effective temperature T_{eff}. Such a schematic diagram is shown in Figure 6. In Figure 6 the dashed vertical lines denote compositions of various alloys. Figurative points corresponding to the effective temperature of the alloys are indicated by an open circle and numbered. Each star with a letter indicates the composition and temperature of an alloy's treatment (normal cooling, SPD or rapid quenching).

The results of the work on HPT of Co-Cu alloys are schematically shown by the points a, b and 2 (Figure 6) [2]. The composition of the supersaturated solid solution of the component B in γ-phase of A corresponds to the point b. This undercooled supersaturated solid solution in the metastable γ-phase is HPT-treated in the point a. After HPT the almost pure α-phase of A is formed as a consequence of γ-α transition. It corresponds to the point 2. The respective $T_{\text{eff}} = 400$°C for the Co-Cu system.

The supersaturated solid solution in the as-cast Al-30 mass% Zn alloy contained about 15 mass% Zn [13, 14]. It corresponds to the point b in Figure 6. The HPT at room temperature (point a) produced nanograined pure Al (point 1) and pure Zn particles simultaneously leading to the unusual softening [13, 14]. The respective $T_{\text{eff}} = 30$°C. The homogenized one-phase solid solutions in the Cu-Ni alloys with 42 and 77 mass% Ni (point 3) decomposed after HPT at room temperature (point a) into Cu-rich and Ni-rich phases [15]. The composition of resulted phases permitted to estimate $T_{\text{eff}} = 200$°C for the Cu-77 mass% Ni alloy and $T_{\text{eff}} = 270$°C for the Cu-42 mass% Ni alloy [15].

The Fe-20 mass% (Nd,Pr)-5 mass% B-1.5 mass% Cu alloy containing crystalline phases [$(Nd,Pr)_2Fe_{14}B$ and Pr-rich phase] transforms after HPT (point c) into a mixture of the amorphous phase and $(Nd,Pr)_2Fe_{14}B$ nanograins [16]. According to the Martin's model this means that the T_{eff} is so high that the configurative point for the treated alloy is in the two-phase area where both solid and liquid phases are present (point 4, Figure 6). The melt appears in the Nd-Fe-B system above eutectic temperature $T_{\text{e}} = 665$°C [17]. It means that the effective temperature is slightly above $T_{\text{e}} = 665$°C and can be estimated as $T_{\text{eff}} = 700$°C.

The coarse-grained as-cast Ni-20 mass% Nb-30 mass% Y and Ni-18 mass% Nb-22 mass% Y alloys contained before HPT the NiY, $NbNi_3$, Ni_2Y, Ni_7Y_2 and Ni_3Y phases (point g) [36, 39]. After HPT these alloys transformed into a mixture of two nanocrystalline NiY and $Nb_{15}Ni_2$ phases and two different amorphous phases (one was Y-rich and another Nb-rich) (point 6). The Ni-Nb-Y phase diagram contains two immiscible melts above 1440°C [93]. Therefore, the effective temperature is slightly above $T_{\text{e}} = 1440$°C and can be estimated as $T_{\text{eff}} = 1450$°C. It is remarkable that the rapid solidification of these alloys from the liquid state (point f) also allows obtaining the mixture of two amorphous phases.

Especially valuable data on the effective temperature of SPD can be extracted from the work on HPT of Ti-48.5 at% Ni, Ti-50.0 at% Ni and Ti-50.7 at% Ni alloys [33]. The HPT of equiatomic Ti-50.0 at% Ni alloy at room temperature (point e) resulted in the fully amorphous state (point 5, $T_{\text{eff}} = 1350$°C, respectively). The HPT of the non-equiatomic Ti-48.5 at% Ni alloy at 270°C (point h) produced the mixture of amorphous and nanocrystalline phases (point 7, $T_{\text{eff}} = 1050$°C). When the HPT temperature of the Ti-48.5 at% Ni alloy increased up to 350°C (point h), only the mixture of nanocrystaline phases formed, without amorphous phase. It means that the corresponding point moved from the position 7 in the $[\delta + \text{L}]$ region into position 8 in the two-phase $[\delta + \gamma]$ region and the effective tempera-

ture decreased to $T_{\rm eff} = 950$°C. The HPT of another non-equiatomic Ti-50.7 at% Ni alloy at 200°C (point j) produced the mixture of amorphous and nanocrystalline phases (point 9, $T_{\rm eff} = 1250$° C). When the HPT temperature of the Ti-50.7 at% Ni alloy increased up to 250°C (point k), only the mixture of nanocrystaline phases formed, without amorphous phase. It means that the corresponding point moved from the position 9 in the [δ+L] region into position 10 in the two-phase $\delta+\beta$ region and the effective temperature decreased to $T_{\rm eff} = 1100$°C. Therefore, it can be clearly seen from the data obtained by Prokoshkin et al. [33] that the increase of the HPT treatment temperature leads to the decrease of $T_{\rm eff}$. It is in full accordance with the equation (1) because the increase of T leads to increase of $D_{\rm b}$, and at the same time the amount of deformation-driven atomic movements characterized by $D_{\rm HPT}$ remains unchanged.

Last group of the results are the experiments on the so-called nanocrystallization. The rapid solidification of these alloys from the liquid state (point d) produces the fully amorphous phase. Afterwards the amorphous phase was subjected to the HPT at room temperature (point c). HPT led to the formation of crystalline nanoparticles in the amorphous matrix (point 4). The position of point 4 in a respective phase diagram slightly above the $T_{\rm e}$ permits to estimate $T_{\rm eff}$. For the nanocrystallized Ni-29 mass% Fe-15 mass% Co-10 mass% B-2 mass% Si alloy [53] our estimation gives $T_{\rm eff} = 1000$°C. For the nanocrystallized Cu-20 mass% Zr-20 mass% Ti alloy [54] $T_{\rm eff} = 700$°C. For the nanocrystallized Al-8 mass% Ce-5 mass% Ni-2 mass% Co alloy [55] $T_{\rm eff} = 400$°C. For the nanocrystallized Fe-6 mass% Si-13 mass% B alloy [56] $T_{\rm eff} = 1100$°C. For the nanocrystallized Zr-5 mass% Ti-20 mass% Cu-10 mass% Al-8 mass% Ni alloy [57] $T_{\rm eff} = 1100$°C. We have to underline again that the effective temperatures determined in this way are much higher than the macroscopic temperature of the SPD-treatment which is usually only slightly above the ambient one. From this pont of view HPT strongly differs for example from the friction stir processing where the part being processed is really "lightening" during the treatment [94–96].

The HPT-treatment in our work at 5 GPa produce the ωZr high-pressure allotrope. Therefore, the usage of equilibrium "temperature - composition" diagrams (like in Figure 6) is not enough to estimate the effective temperature of SPD. As we already mentioned above, the high pressure always decreases the diffusivity and grain boundary mobility [90, 91]. It means that in order to explain the increased atomic fluxes during SPD we need the increased $T_{\rm eff}$, and we have to search for the respective phases in the "temperature – pressure" or even the "temperature – pressure – composition" phase diagrams.

In Figure 7 the "temperature – pressure " phase diagrams is shown for the Ti, Zr and Hf obtained in static experiments with the nearly-hydrostatic conditions [64–76]. These diagrams for Ti, Zr and Hf are homologous. In all three metals

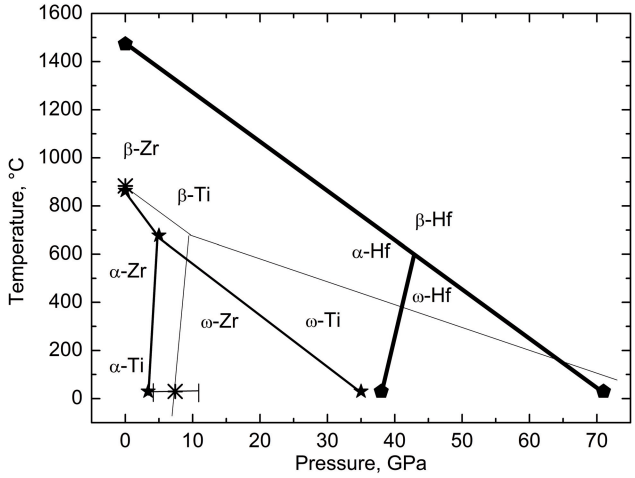

Figure 7. "Temperature – pressure" equilibrium phase diagram for titanium (crosses, thin lines), zirconium (stars, middle-thick lines) and hafnium (pentagons, thick lines).

the high-pressure ω-phase (C32) appears at room temperature. The ωZr phase becomes stable at room temperature above 3.4 GPa (star) [69]. Various room-temperature experiments for Ti have shown a transition from α to the ω phase at a pressure of 11.9 GPa [63], 2–7 GPa [64], 2.9–7.5 GPa [65, 66], or 8 GPa (double cross with horizontal error bar) [67, 68].The ωHf appears above 38 GPa (pentagon [67, 68]. The temperature of $\alpha \leftrightarrow \beta$ transition decreases with increasing pressure. After the $\alpha/\beta/\omega$ triple point the temperature of $\omega \leftrightarrow \beta$ transition continues to decrease with increasing pressure. The α/β and ω/β equilibrium lines for Ti are positioned at higher temperature than that for Zr. In turn, the α/β and ω/β equilibrium lines for Hf lie even higher. The transitions from ω to β phase at room temperature proceed in Ti above 87 GPa [67, 68], in Zr at [35 $\pm$ 3] GPa [75, 76] and in Hf at 71 GPa [67, 68].

In Figure 8 the conditions of HPT (small full symbols) and the estimated values of effective temperatures (large open symbols) are shown for Ti, Zr and Hf. The starting α-phase in 99.8 mass% pure Zr [46] and commercially pure Zr [48] transforms into the $\omega + \beta$ mixture after HPT with 1 rpm and 5 rotations at 3 and 6 GPa (full squares, Figure 8b) [46, 48]. This fact permits to estimate the $T_{\rm eff}$ at the ω/β equilibrium line as 650°C (open square). After HPT at 1 GPa [46,48,97], 2 GPa [46,50], 3 and 4 GPa [46] the α-phase does not transform in other phase(s). It does not permit to estimate the effective temperature of HPT process. The HPT at 6, 14, 22, 30 and 40 GPa with 1 rpm and 5 rotations (small full pentagons) transforms the starting α-phase into ω-phase [50]. However, the ω-phase is in equilibrium at room temperature above 3.4 GPa (star) [69]. Therefore, one cannot estimate the effective temperature using these results. The HPT of an Zr-2.5 mass% Nb alloy at 0.25, 0.5 and 5 GPa with 0.2 rpm and 5 rotations (full circles) permits

to transform the starting α-phase into the $\alpha + \beta + \omega$ phase mixture [44]. This mixture can be found in the $\alpha + \beta + \omega$ triple point at 670°C (large open circle). In our work the HPT of Zr-2.5 mass% Nb and Zr-8 mass% Nb finishes in the $\beta + \omega$ mixture, almost without α-phase. Also, the addition of Nb decreases the temperature of α-β transition at ambient pressure (see also phase diagram in Figure 3). One can suppose that the temperature of α-β (and ω-β) transition decreases in Zr-Nb alloys also at high pressures. The dashed lines starting in stars at 0.1 MPa show this shift for 2.5 and 8 mass% Nb. The respective effective temperatures are shown by large open squares and are $T_{\text{eff}} = 620$°C for Zr-2.5 mass. % Nb and $T_{\text{eff}} = 550$°C for Zr-8 mass% Nb.

Figure 8a shows the results of the estimation of the effective temperature(s) for titanium. After HPT at room temperature at 1.5 GPa [51, 81], 2 GPa [46, 51], 3, 4 GPa [51], and 5 GPa [51, 98–100] the α-phase does not transform in other phase(s) (full diamonds in Figure 8a). The α-phase remains α-phase also after HPT at 6 GPa with 10 rotations performed at 20, 70, 200, 300, 350, 400 and 450°C [100]. These experiments do not permit to estimate the effective temperature of HPT process. The HPT at 6, 14, 21, 28 and 40 GPa with 0.2 rpm and 5 rotations (small full pentagons) transforms the starting α-phase into ω-phase [51]. However, the ωTi is in equilibrium at room temperature above 7.4 ± 5 GPa (star) [63–68]. Therefore, one cannot estimate the effective temperature using these results. Only in the work of Y. Ivanisenko et al. [52] on HPT of titanium (where the starting α-phase transformed into the $\alpha + \omega$ mixture) permits to estimate the effective temperature. The HPT of commercially pure Ti have been performed with 1 rpm at 3, 4 and 5 GPa with 5 rotations and at 6 GPa with 0.5, 1, 5 and 10 rotations. The amount of ω-phase increased both with increasing pressure (at constant rotation number) and with increasing rotation number (at constant pressure) [52]. The mixture of α and ω phases have been obtained also after HPT at room temperature at 5 GPa, 0.2 rpt, up to 10 rotations [81]. The large open triangle at $T_{\text{eff}} = 400$°C shows the position in the phase diagram which corresponds to the transformations observed in References [52, 81].

Figure 8c shows the results of the estimation of the effective temperature for hafnium. In the work of Edalati et al. [49] the pure Hf (99.99%) have been processed by HPT under pressures of 4 and 30 GPa. X-ray diffraction analysis showed that, unlike Ti and Zr, no ω-phase formation is detected after HPT processing even under a pressure of 30 GPa. It is easy to understand (Figure 8c) because both

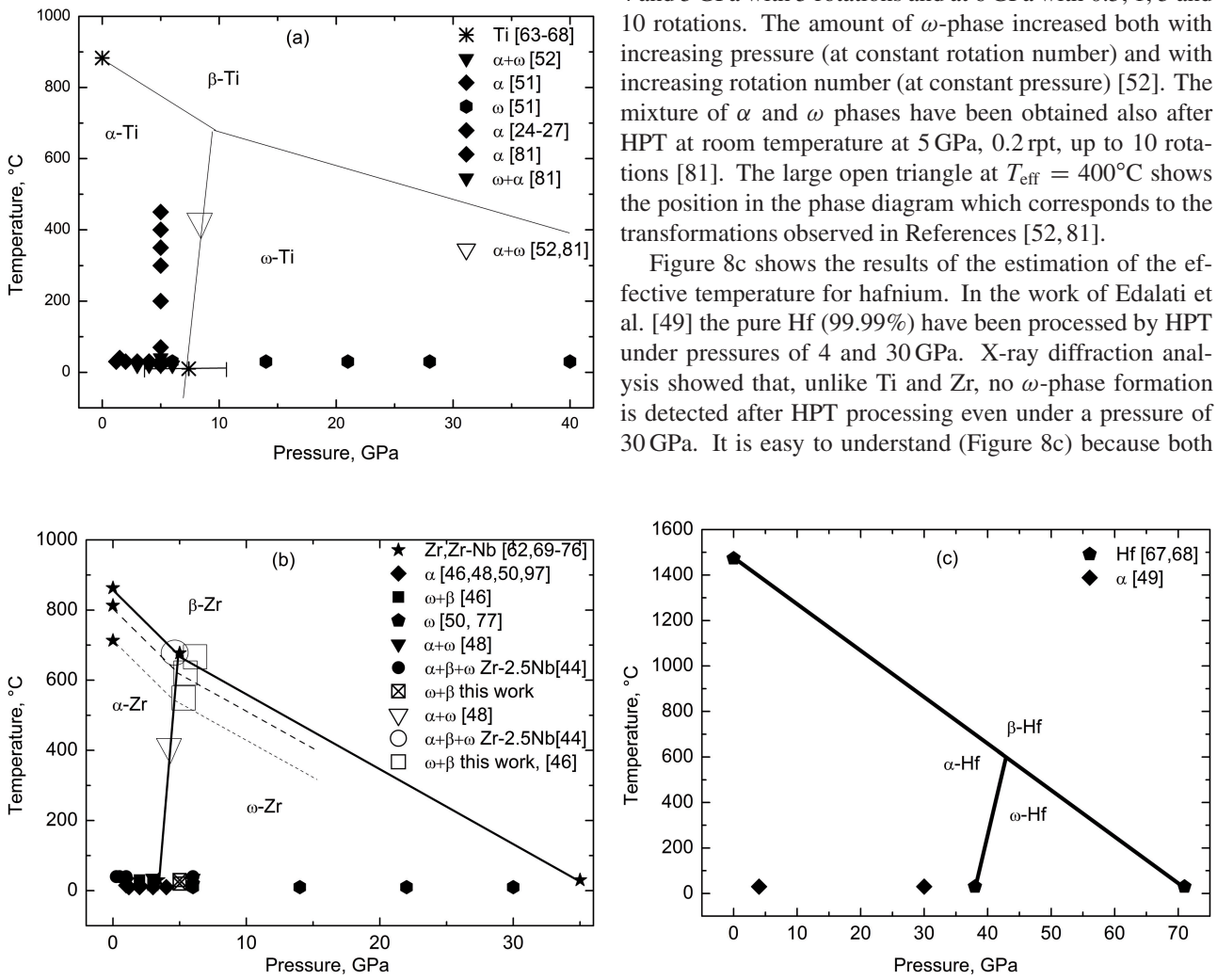

Figure 8. "Temperature – pressure" equilibrium phase diagrams with data for HPT-experiments for (a) titanium (crosses, thin lines), (b) zirconium and (c) hafnium. Small full symbols mark the conditions of HPT-treatment and demonstrate the phases present in the samples after HPT. Large open symbols mark the effective temperatures in the respective phase fields. Diamonds are for the pure α-phase. Circles are for the $\alpha + \omega + \beta$ mixture. Triangles are for the $\alpha + \omega$ mixture. Squares are for the $\omega + \beta$ mixture. Hexagones are for the pure ω-phase.

pressures are below the αHf$\leftrightarrow$ ωHf equilibrium transition pressure at room temperature 38 GPa (pentagon) [67, 68]. Generally, the comparison given above shows that HPT of Ti, Zr or Hf at a certain pressure $P_{\rm HPT}$ do not produce any phases which are reported in static experiments at higher pressures $P_{\rm stat} > P_{\rm HPT}$. On the contrary, the HPT of Ti, Zr or Hf at room temperature $T_{\rm HPT} = T_{\rm room}$ easily produce the phases which can be found in the equilibrium phase diagrams at higher temperature $T_{\rm eff} > T_{\rm HPT}$. It is easy to understand this trend if we recollect that SPD forces the atomic movements (or shuffling) in addition to the conventional thermal diffusion. This forced "diffusion" at $T_{\rm room}$ is then equivalent to the conventional thermal diffusion at higher temperatures $T_{\rm eff} > T_{\rm room}$. Contrary to the increasing temperature, the increasing pressure slows down the diffusion and grain boundary migration [90, 91]. Therefore, the forced atomic movement during HPT produces the states equivalent to higher temperature, but not to the higher pressure.

5 Conclusions

(1) Severe plastic deformation by HPT leads to the phase transitions and strong grain refinement in Zr-Nb alloys.

(2) The starting αZr-phase transforms into $\beta + \omega$ mixture and remains quenched in both studied alloys at the ambient pressure.

(3) The high-pressure ωZr-phase disappears by heating only between 400 and 500°C.

(4) The obtained $\beta + \omega$ phase mixture can be found in the equilibrium phase diagram at higher (effective) temperature ($T_{\rm eff} = 620$°C for Zr-2.5 mass% Nb and $T_{\rm eff} = 550$°C for Zr-8 mass% Nb).

(5) The published papers on phase transitions during HPT are analyzed and the values of effective temperature are estimated.

(6) Contrary to the increasing temperature, the increasing pressure slows down the diffusion and grain boundary migration. Therefore, the forced atomic movement during HPT produces the states equivalent to higher temperature, but not to the higher pressure.

Acknowledgments

Authors thank the Russian Foundation for Basic Research (grants 10-02-00086, 11-03-00029 and 11-08-90439) and Ukrainian Fundamental Research State Fund (grant φ28.2107) for their financial support.

References

[1] G. Martin, *Phys. Rev. B*, **30** (1984), 1424–1436.

[2] B. B. Straumal, A. A. Mazilkin, B. Baretzky, E. Rabkin and R. Z. Valiev, *Mater. Trans.* **53** (2012), 63–71.

[3] X. Sauvage, A. Chbihi and X. Quelennec, *J. Phys.*, **240** (2010), 012003.

[4] H. W. Zhang, S. Ohsaki, S. Mitao, M. Ohnuma and K. Honoa, *Mater. Sci. Eng. A* , **421** (2006), 191–199.

[5] W. Lojkowski, M. Djahanbakhsh, G. Burkle, S. Gierlotka, W. Zielinski and H. J. Fecht, *Mater. Sci. Eng. A*, **303** (2001), 197–208.

[6] K. Hono, M. Ohnuma, M. Murayama, S. Nishida, A. Yoshie and T. Takahashi, *Scripta Mater.*, **44** (2001), 977–983.

[7] A. Taniyama, T. Takayama, M. Arai and T. Hamada, Scripta Mater., **51** (2004), 53–58.

[8] V. G. Gavriljuk, *Mater. Sci. Eng. A*, **345** (2003), 81–89.

[9] X. Sauvage, X. Quelennec, J. J. Malandain and P. Pareige, *Scripta Mater.*, **54** (2006), 1099–1103.

[10] V. A. Teplov, V. P. Pilugin, V. S. Gaviko and E. G. Chernyshov, *Phil. Mag. B*, **68** (1993), 877–881.

[11] V. V. Stolyarov, R. Lapovok, I. G. Brodova and P. F. Thomson, *Mater. Sci. Eng. A*, **357** (2003), 159–167.

[12] X. Sauvage, F. Wetscher and P. Pareige, *Acta Mater.*, **53** (2005), 2127–2135.

[13] B. B. Straumal, B. Baretzky, A. A. Mazilkin, F. Phillipp, O. A. Kogtenkova, M. N. Volkov and R. Z. Valiev, *Acta Mater.*, **52** (2004), 4469–4478.

[14] A. A. Mazilkin, B. B. Straumal, E. Rabkin, B. Baretzky, S. Enders, S. G. Protasova, O. A. Kogtenkova and R. Z.Valiev, *Acta Mater.*, **54** (2006), 3933–3939.

[15] B. B. Straumal, S. G. Protasova, A. A. Mazilkin, E. Rabkin, D. Goll, G. Schütz, B. Baretzky and R. Z. Valiev, *J. Mater. Sci.*, **47** (2012), 360–367.

[16] C. M. Cepeda-Jiménez, J. M. García-Infanta, A. P. Zhilyaev, O. A. Ruano and F. Carreño, *J. Alloys Comp.*, **509** (2011), 636–643.

[17] Y. Ivanisenko, I. MacLaren, X. Sauvage, R. Z. Valiev and H.-J. Fecht, *Acta Mater.*, **54** (2006), 1659–1669.

[18] X. Sauvage and Y. Ivanisenko, *J. Mater. Sci.*, **42** (2007), 1615–1621.

[19] Y. Ivanisenko, W. Lojkowski, R. Z. Valiev and H. J. Fecht, *Acta Mater.*, **51** (2003), 5555–5570.

[20] V. V. Sagaradze, S. V. Morozov, V. A. Shabashov, L. N. Romashev and R. I. Kuznetsov, *Phys. Met. Metall.*, **66** (1988), 328–338.

[21] B. B. Straumal, A. A. Mazilkin, S. G. Protasova, S. V. Dobatkin, A. O. Rodin, B. Baretzky, D. Goll and G. Schütz, *Mater. Sci. Eng. A*, **503** (2009), 185–189.

[22] V. V. Sagaradze and V. A. Shabashov, *Nanostruct. Mater.*, **9** (1997), 681–684.

[23] M. Murayama, K. Hono and Z. Horita, *Mater. Trans. - JIM*, **40** (1999), 938–941.

[24] S. Ohsaki, S. Kato, N. Tsuji, T. Ohkubo and K. Hono, *Acta Mater.*, **55** (2007), 2885–2895.

[25] X. Sauvage and R. Pippan, *Mater. Sci. Eng. A*, **410–411** (2005), 345–347.

[26] X. Sauvage, C. Genevois, G. Da Costa and V. Pantsyrny, *Scripta Mater.*, **61** (2009), 660–663.

[27] X. Sauvage, W. Lefebvre, C. Genevois, S. Ohsaki and K. Hono, *Scripta Mater.*, **60** (2009), 1056–1061.

[28] B. B. Straumal, S. V. Dobatkin, A. O. Rodin, S. G. Protasova, A. A. Mazilkin, D. Goll and B. Baretzky, *Adv. Eng. Mater.*, **13** (2011), 463–469.

[29] A. V. Korznikov, O. Dimitrov, G. F. Korznikova, J. P. Dallas, A. Quivy, R. Z. Valiev and A. Mukherjee, *Nanostruct. Mater.*, **11** (1999), 17–23.

[30] A. V. Korznikov, G. Tram, O. Dimitrov, G. F. Korznikova, S. R. Idrisova and Z. Pakiela, *Acta Mater.*, **49** (2001), 663–671.

[31] C. Rentenberger and H. P. Karnthaler, *Acta Mater.*, **56** (2008), 2526–2530.

[32] A. V. Sergueeva, C. Song, R. Z. Valiev and A. K. Mukherjee, *Mater. Sci. Eng. A*, **339** (2003), 159–165.

[33] S. D. Prokoshkin, I.Yu. Khmelevskaya, S. V. Dobatkin, I. B. Trubitsyna, E. V. Tatyanin, V. V. Stolyarov and E. A. Prokofiev, *Acta Mater.*, **53** (2005), 2703–2714.

[34] X. Sauvage, L. Renaud, B. Deconihout, D. Blavette, D. H. Ping and K. Hono, *Acta. Mater.*, **49** (2001), 389–394.

[35] T. Miyazaki, D. Terada, Y. Miyajima, C. Suryanarayana, R. Murao, Y. Yokoyama, K. Sugiyama, M. Umemoto, T. Todaka, N. Tsuji, Nobuhiro, *J. Mater. Sci.*, **46** (2011), 4296–4301.

[36] A. A. Mazilkin, G. E. Abrosimova, S. G. Protasova, B. B. Straumal, G. Schütz, S. V. Dobatkin and A. S.Bakai, *J. Mater. Sci.*, **46** (2011), 4336–4342.

[37] V. V. Stolyarov, D. V. Gunderov, A. G. Popov, V. S. Gaviko and A. S.Ermolenko, *J. Alloys Comp.*, **281** (1998), 69–71.

[38] Y. Matsuura, S. Hirosawa, H. Yamamoto, S. Fujimira, M. Sagawa and K. Osamura, *Jap. J. Appl. Phys. Part 2 – Lett.*, **24** (1985), L635–L637.

[39] B. B. Straumal, A. A. Mazilkin, S. G. Protasova, D. Goll, B. Baretzky, A. S Bakai and S. V. Dobatkin, *Kovove Mater. – Metall. Mater.*, **49** (2011), 17–22.

[40] Á. Révész, S. Hóbor, J. L. Lábár, A. P. Zhilyaev and Zs. Kovácz, *J. Appl. Phys.*, **100** (2006), 103522.

[41] I. MacLaren, Y. Ivanisenko, R. Z. Valiev and H. J. Fecht, *J. Phys.*, **26** (2006), 335–338.

[42] Y. Ivanisenko, I. MacLaren, X. Sauvage, R. Z. Valiev and H. J. Fecht, *Sol. State Phen.*, **114** (2006), 133–144.

[43] Y. Ivanisenko, I. MacLaren, X. Sauvage, R. Z. Valiev and H. J. Fecht, *Acta Mater.*, **54** (2006), 1659–1669.

[44] A. P. Zhilyaev, I. Sabirov, G. González-Doncel, J. Molina-Aldareguía, B. Srinivasarao and M. T. Pérez-Prado, *Mater. Sci. Eng. A*, **528** (2011), 3496–3505.

[45] A. P. Zhilyaev, A. V. Sharafutdinov and M. T. Pérez-Prado, *Adv. Eng. Mater.*, **12** (2012), 754–757.

[46] A. P. Zhilyaev, F. Gálvezc, A. V. Sharafutdinov and M. T. Pérez-Prado, *Mater. Sci. Eng. A*, **527** (2010), 3918–3928.

[47] M. T. Pérez-Prado, A. V. Sharafutdinov and A. P. Zhilyaev, *Mater. Lett.*, **64** (2010), 211–214.

[48] M. T. Pérez-Prado and A. P. Zhilyaev, *Phys. Rev. Lett.*, **102** (2009), 175504.

[49] K. Edalati, Z. Horita and Y. Mine, *Mater. Sci. Eng. A*, **527** (2010), 2136–2141.

[50] K. Edalati, Z. Horita, S. Yagi and E. Matsubara, *Mater. Sci. Eng. A*, **523** (2009), 277–281.

[51] K. Edalati, E. Matsubara and Z. Horita, *Metal Mater Trans A*, **40** (2009), 2079–2086.

[52] Y. Ivanisenko, A. Kilmametov, H. Roesner and R. Z. Valiev, *Int. J. Mater. Res.*, **99** (2008), 36–41.

[53] A. M. Glezer, M. R. Plotnikova, A. V. Shalimova and S. V. Dobatkin, *Bull. Russ. Ac. Sci. Phys.*, **73** (2009), 1233–1236.

[54] S. Hóbor, Á. Révész, A. P. Zhilyaev and Zs. Kovácz, *Rev. Adv. Mater. Sci.*, **18** (2008), 590–592.

[55] Zs. Kovács, P. Henits, A. P. Zhilyaev and Á.Révész, *Scripta Mater.*, **54** (2006), 1733–1737.

[56] G. E. Abrosimova, A. S. Aronin, S. V. Dobatkin, S. D. Kaloshkin, D. V. Matveev, O. G. Rybchenko, E. V. Tatyanin and I. I. Zverkova, *J. Metastab. Nanocryst. Mater.*, **24** (2005), 69–72.

[57] Á. Révész, E. Schafler and Zs. Kovács, *Appl. Phys. Lett.*, **92** (2008), 011910.

[58] S. Hóbor, Zs. Kovács, A. P. Zhilyaev, L. K. Varga, P. J. Szabó and Á. Révész, *J. Phys.*, **240** (2010), 012153.

[59] S. Hóbor, Á. Révész, P. J. Szabó, A. P. Zhilyaev, V. Kovács Kis, J. L. Lábár and Zs. Kovács, *J. Appl. Phys.*, **104** (2008), 033525.

[60] P. Henits, Á. Révész, A. P. Zhilyaev and Zs. Kovács, *J. Alloys Comp.*, **461** (2008), 195–199.

[61] Zs. Kovács, P. Henits, A. P. Zhilyaev, N. Q. Chinh and Á. Révész, *Mater. Sci. Forum*, **519–521** (2006), 1329–1334.

[62] *Binary alloy phase diagrams*, edited by T. B. Massalski, 2nd ed. ASM International, Materials Park, OH, (1990).

[63] A. R. Kutzar, *JETP Lett.* **35** (1982), 108–112.

[64] S. K. Sikka, Y. K. Vohra and R. Chidambaram, *Prog. Mater. Sci.*, **27** (1982), 245–310.

[65] J. C. Jamieson *Science*, **140** (1963), 72–73.

[66] A. Jayaraman, W. Clement and G. C. Kennedy, *Phys. Rev.*, **131** (1963), 644–649.

[67] H. Xia, A. L. Ruoff and Y. K.Vohra, *Phys. Rev. B*, **44** (1991), 10374–10376.

[68] H. Xia, G. Parthasarathy, H. Luo, Y. K. Vohra and A. L. Ruoff, *Phys. Rev. B*, **42** (1990), 6736–6738.

[69] J. Zhang, Y. Zhao, P. A. Rigg, R. S. Hixson and G. T. Gray III, *J. Phys. Chem. Solids*, **68**, 2297–2302.

[70] J. Zhang, Y. Zhao, C. Pantea, J. Qian, P. Rigg, R. Hixson, G. T. Gray, Y. Yang, L. Wang and Y. Wang, *J. Phys. Chem. Solids*, **66** (2005), 1213–1219.

[71] Y. K. Vohra, *J. Nucl. Mater.*, **75** (1978), 288–293.

[72] B. Srinivasarao, A. P. Zhilyaev and M. T. Pérez-Prado, *Scripta Mater.*, **65** (2011), 241–244.

[73] B. Olinger and J. C. Jamieson *High Temp. High Press.*, **5** (1973), 123–128.

[74] S. K. Sikka, Y. K. Vohra and R. Chidambaram, *Prog. Mater. Sci.*, **27** (1982), 245–310.

[75] J. Zhang, Y. Zhao, C. Pantea, J. Qian, P. Rigg, R. Hixson, G. T. Gray, Y. Yang, L. Wang and Y.Wang, *J. Phys. Chem. Solids*, **66** (2005), 1213–1219.

[76] H. Xia, S. J. Duclos, A. L. Ruoff and Y. K.Vohra, *Phys. Rev. Lett.*, **64**, 204.

[77] M. T. Pérez-Prado, A. A. Gimazov, O. A. Ruano, M. E. Kassner and A. P. Zhilyaev, *Scripta Mater.*, **58** (2008), 219–222.

[78] N. M. Beskorovainyi, B. A. Kalin, P. A. Platonov, and I. I. Chernov. *Structural materials for nuclear reactors.*, Energoatomisdat, Moscow, (1995).

[79] L. B. Zuev, B. S. Semukhin and S. Y.Zavodchikov, *Mater. Lett.*, **57** (2005), 1015–1020.

[80] L. Saldaòa, A. Méndez-Vilas, L. Jiang, M. Multigner, J. L. González-Carrasco, M. T. Pérez-Prado, M. L. González-Martín, L. Munuera and N. Vilaboa, *Biomaterials* **28** (2007), 4343–4354.

[81] I. Todaka, J. Sasaki, T. Moto and M. Umemoto, *Scripta Mater.*, **59** (2008), 615–618.

[82] T. Ungar and A. Borbely, *Appl. Phys. Lett.*, **69** (1996), 3173–3175.

[83] A. F. Guillermet, *Z. Metallkde*, **82** (1991), 478–487.

[84] J.-O. Andresson, T. Helander, L. Höglund, P. Shi and B. Sundman, *Calphad*, **26** (2002), 273–312.

[85] B. B. Straumal, A. S. Gornakova, Y. O. Kucheev, B. Baretzky and A. N. Nekrasov, *J. Mater. Eng. Performance*, **21** (2012), 721–724.

[86] S. K. Sikka, Y. K. Vohra, R. Chidambaram, *Progr. Mater. Sci.*, **27** (1982), 245–310.

[87] B. B. Straumal, A. S. Gornakova, A. A. Mazilkin, O. B. Fabrichnaya, M. J. Kriegel, B. Baretzky, J.-Z. Jiang and S. V. Dobatkin, *Mater. Lett.*, **71** (2012), DOI: 10.1016/j/matlet.2012.04.153.

[88] R. Davis, H. M. Flower and D. R. F.West, *J. Mater. Sci.***14** (1975), 712–722.

[89] S. Neogy, K. V. M. Krishna, D. Srivastava and G. K. Dey, *Phil. Mag.*, **91** (2011), 4447–4464.

[90] F. J. Kedves and G. Erdélyi, *Diff. Def. Forum*, **66–69** (1989), 175–188.

[91] D. A. Molodov, B. B. Straumal and L. S. Shvindlerman, *Scripta metal.*, **18** (1984), 207–211.

[92] G. Thomas, H. Mori and H. Fujita, *Scripta Metall.*, **16** (1982), 589–592.

[93] N. Mattern, U. Kühn, A. Gebert, A. Schoeps, T. Gemminga and L. Schultz, *Mater. Sci. Eng. A*, **449/451** (2007), 207–210.

[94] S. Swaminathan, K. Oh-Ishi, A. P. Zhilyaev, Ch.B. Fuller, B. London, M. W. Mahoney and T. R. McNelley, *Metal. Mater. Trans. A*, **41** (2010), 631–640.

[95] T. Giles, K. Oh-Ishi, A. P. Zhilyaev, S. Swaminathan, M. W. Mahoney and T. R. McNelley, *Metal. Mater. Trans. A*, **40** (2009), 104–115.

[96] K. Oh-Ishi, A. P. Zhilyaev and T. R. McNelley, *Metal. Mater. Trans. A*, **37** (2006), 2239–2251.

[97] A. V. Sergueeva, V. V. Stolyarov, R. Z. Valiev and A. K. Mukherjee, *Scripta Mater.*, **45** (2001), 747–752,

[98] R. Z. Valiev, A. V. Sergueeva and A. K. Mukherjee, *Scripta Mater.*, **49** (2003), 669–674.

[99] R. K. Islamgaliev, V. U. Kazyhanov, L. O. Shestakova, A. V. Sharafutdinov and R. Z. Valiev, *Mater. Sci. Eng. A*, **493** (2008), 190–194.

[100] I. Todaka, M. Umemoto, A. Yamazaki, J. Sasaki and K. Tsuchiya, *Mater. Trans.*, **49** (2008), 47–53.